Particle & Particle Systems Characterization
www.particle-journal.com

In Situ Dimensional Characterization of Magnetic Nanoparticle Clusters during Induction Heating

*Hayden Carlton, Kathryn Krycka, Markus Bleuel, and David Huitink**

The study and fundamental understanding of magnetic nanoparticle induction heating remains critical for the advancement of magnetic hyperthermia technologies. Complete characterization of not only the nanoparticles themselves but their interparticle behavior in a sample matrix is necessary to accurately predict their heating response. Herein, an in situ method for measuring the extent of nanoparticle clustering during induction heating using small-angle and ultrasmall-angle neutron scattering facilities at the National Institute of Standards and Technology Center for Neutron Research is described and implemented by comparing two sets of iron oxide nanoparticles with differing structures and magnetic properties. By fitting the scattering profiles to a piecewise model covering a wide Q-range, the magnitude of nanoparticle clustering during induction heating is quantified. Observations of the low-Q intensity before and after heating also allow for relative measurement of the cluster volume fraction during heating. The use of this method can prove to be advantageous in both developing more encompassing models to describe magnetic nanoparticle dynamics during heating as well as optimizing nanoparticle synthesis techniques to reduce aggregation during heating.

1. Introduction

Iron oxide nanoparticles (IONPs) offer a range of potential engineering solutions in applications such as multimodal imaging,[1] cancer treatment,[2] and targeted drug delivery.[3] Arguably, the most researched topic involving the multifunctional nature of IONPs continues to be their application in magnetic nanoparticle hyperthermia (MNH), in which localized nanoparticle induction heating can facilitate targeted tumor treatment. MNH can often be coupled with standard tumor therapies to not only damage the cancerous cells with applied heat but also reduce the tumor cells' resistance to standard treatment therapies, such as ionizing radiation.[4,5]

There still exists a push in the scientific community to understand the dynamics of IONPs under an alternating magnetic field in order to optimize their thermal output. Thermal performance of IONPs is typically characterized using a quantity called the specific absorption rate (SAR), which represents the thermal output per unit mass of nanoparticles in a surrounding medium. SAR can be calculated experimentally by observing the temperature rise of the bulk medium during induction heating, where the surrounding environment is assumed to be adiabatic. A myriad of nanoparticle structural characteristics have been discovered to have profound effects on SAR, with the majority of the studies being focused on nanoparticle size,[6] shape,[7] and capping chemistry.[8] While individual IONP structure governs a large part of their heating response, colloidal properties of IONP suspensions, specifically concentration, have been observed to impact SAR as well.[9] Most early efforts focused on describing systems of noninteracting particles;[10] however, recent computational and experimental research has emphasized the role of interparticle interactions and how they impact SAR – mostly in a negative sense.[5,11] These numerous studies and their associated experimental variables demonstrating the intermodal relationship of size, concentration, capping chemistry, etc., evidence the existence of the strong dependence of SAR on colloidal properties. As such, understanding the full breadth of how those properties affect IONP heating performance is paramount for the advancement of MNH.

Depending on the fluid, nanoparticle structure, and magnetic field properties, interacting particles within an alternating magnetic field can induce the formation of larger structures during heating, such as chains or clusters, which can span over much larger length scales[9,12] and can be amplified or augmented through the use of specialized capping agents.[13] IONPs are almost always coated with a capping agent or other surface functionalization to reduce localized aggregation; previous research illustrates the detrimental effects that aggregation has on SAR in biological media.[14] Quantifying the extent of IONP clustering during induction heating is key to the development

H. Carlton, Dr. D. Huitink
Mechanical Engineering Department
University of Arkansas
863 W. Dickson St., Fayetteville, AR 72701, USA
E-mail: dhuitin@uark.edu
Dr. K. Krycka, Dr. M. Bleuel
NIST Center for Neutron Research
National Institute of Standards and Technology
Gaithersburg, MD 20899-8562, USA
Dr. M. Bleuel
Department of Materials Science and Engineering
University of Maryland
College Park, MD 20742-2115, USA
The ORCID identification number(s) for the author(s) of this article can be found under https://doi.org/10.1002/ppsc.201900358.

DOI: 10.1002/ppsc.201900358

of better capping agents for MNH applications as well as to create more stable IONP colloids. Methods such as magnetic force and electron microscopy offer some ability as ex situ methods for characterizing nanoparticle groupings, but they both typically require the drying of the IONPs on a substrate, which may induce unwanted aggregation. More advanced techniques for quantifying nanoparticle aggregation and particle size distribution include asymmetric flow field fractionation[15] and variations of ion mobility spectrometry;[16] however neither would be able to provide measurements during an induction heating cycle. Small-angle neutron scattering (SANS) methods have been proven experimentally to be valid approaches to measuring the bulk size characteristics of IONPs suspended in water or deuterium oxide, as well as maintaining the submicrometer resolution necessary to characterize internal magnetic domain structure within an individual nanoparticle.[17] However, the majority of previous experiments using SANS in this manner have done so with static magnetic fields; an exception to this statement can be seen in the study by Bender et al. in their time-dependent SANS analysis of Ni nanorod colloids in an oscillating magnetic field.[18] In this article, we intend to describe the incorporation of an induction heating coil into a neutron beamline as one of the first in situ methods for characterizing long-range IONP cluster formations during induction heating using SANS and ultrasmall-angle neutron scattering (USANS) techniques. Two different sets of IONPs will be analyzed under a high frequency alternating magnetic field and fit to existing SANS/USANS models to illustrate their respective clustering behavior.

2. SANS/USANS Modeling

Small-angle scattering measurements are typically represented with respect to the scattering wavevector, Q; assuming that the neutron scatters elastically, Q equates to the transfer of momentum in the scattered neutron, which is related to the scattering angle. The magnitude of Q also correlates with the real space length (d) of the object from which the neutron scatters $\left(d = \frac{2\pi}{Q}\right)$. A piecewise model comprised of three different submodels fits all of the scattering intensity data gathered with SANS and USANS, which aided in interpreting the geometry of our samples during an induction heating cycle. Utilizing all of the submodels allowed for the IONPs to be characterized over a broad Q-range, which in turn correlates with a broad range in real space. The pearl necklace model provided information regarding the geometry of local IONP groupings (<150 nm), a power law representation described cluster fractal properties (150 nm–3.6 μm), and the Guinier–Porod model measured relative cluster size and dimension (3.6–15 μm). A visual representation of the entire model used in this study as well as a diagram of which aspect of the clusters were probed in each submodel is illustrated in **Figure 1**. Complete mathematic representations of each model can be found in the Supporting Information.

The pearl necklace submodel fits the data within the Q-range of $Q > 4 \times 10^{-3}$ Å^{-1}, which were gathered with the NG7 SANS instrument.[19] As outlined in the articles by Schweins and

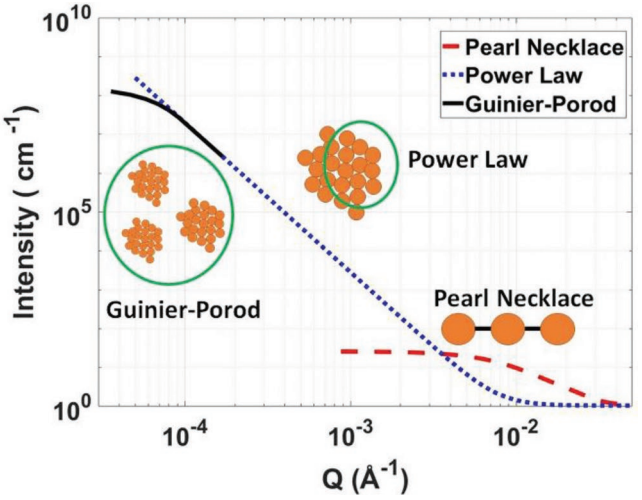

Figure 1. Visual depiction of the piecewise model used, with illustrations for each region. The pearl necklace describes the local groupings; the power law model provides information regarding the nanoparticle clusters, specifically dealing with their fractal dimension. The Guinier–Porod model extends to the lowest Q-range (largest real space range), and it determines the size extent of the clusters formed during heating.

Huber and Chen and Teixeira, the pearl necklace model provided a form factor for a colloidal system of N spheres joined together by M uniform rods. The use of the pearl necklace model in analyzing colloidal suspensions has previously extended into research involving the analysis of ferrofluids using polarized SANS.[20] Bonini et al. assumed that the majority of their scattering intensity would come from the nanoparticles themselves (pearls) versus the interparticle linkages (necklace). In the case of IONP systems, these linkages represent the magnetic moment interactions between neighboring particles. It was assumed that the same approximation would be valid for the IONP systems used in this study.

The mid-Q power law model bridged the gap between the SANS and USANS data fitting (1.732×10^{-4} Å^{-1} < Q < 4×10^{-3} Å^{-1}). Power law data fitting is used ubiquitously in small-angle scattering experiments, with arguably the most common implementation being in the widely known, empirical Guinier–Porod model.[21] In the general case, a power law defines the "Porod region" of the Guinier–Porod model, which interprets the complexity of a system of objects. The key parameter extracted from the power law fitting is the slope (n), which can be used to describe the system's fractal properties. The aforementioned pearl necklace model interprets the IONP suspensions as a system of cross-linking nanoparticle chains joined together by magnetic interactions, which can be viewed as a mass fractal. If $n = 2$, this is indicative of Gaussian chain formation in the suspensions, while $2 < n < 3$ represents a much more clustered network of chains. The slope can also depict the surface fractal dimension of IONP clusters, which is particularly useful in studying large-scale nanoparticle clustering. Values of n between 3 and 4 correlate to the relative roughness of the cluster's surface, with $n = 4$ being a "smooth" surface. In this case, if it is assumed that D represents the commonly used fractal dimension term, then $n = 6 - D$.[22]

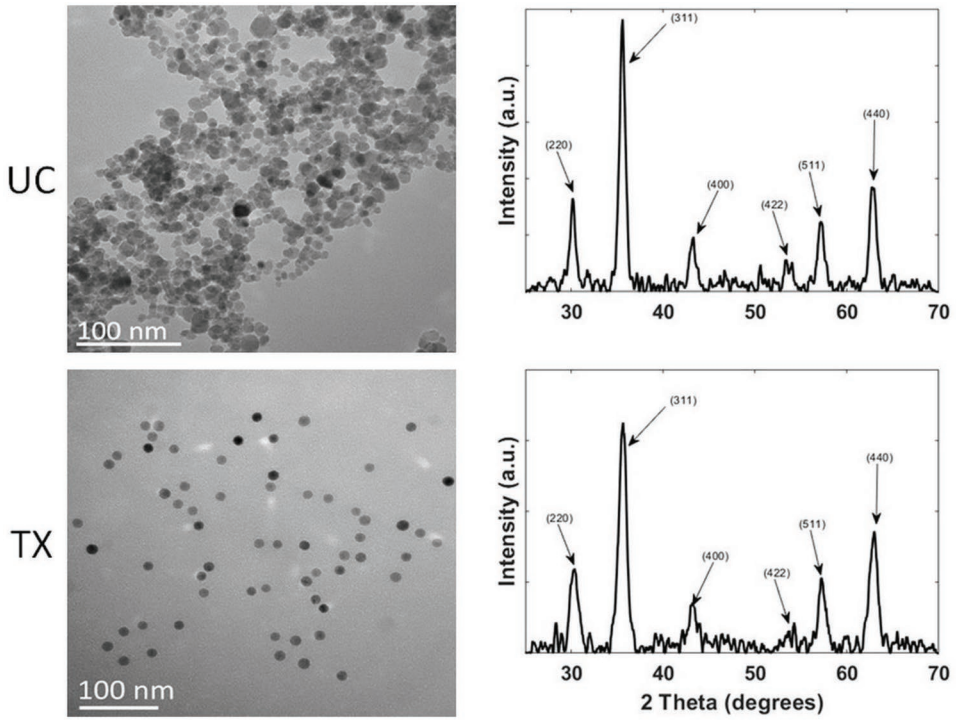

Figure 2. Visual and crystallographic characterization of the TX and UC IONPs.

The submodel for the lowest-Q region ($Q < 1.732 \times 10^{-4}$ Å^{-1}) fits the data gathered by BT5 USANS to the Guinier–Porod model; however, in this case, the area of interest was the Guinier region, which provides useful information regarding the size range and geometry of a system of objects by analyzing the radius of gyration as well as the dimension variable.[21] In terms of the IONPs, this aspect of the model described not only the size of the IONP clusters but also their relative shape (spherical, rod-shaped, planar, etc.).

3. Results and Discussion

3.1. IONP Characterization

Coprecipitation synthesis methods created two sets of IONPs in this effort: uncapped (UC) IONPs and TX-100-stabilized (TX) IONPs. Transmission electron microscopy (TEM) and X-ray diffraction (XRD) provided visual and crystalline characterization of IONPs; **Figure 2** displays the results of this characterization. Both the sets of IONPs exhibited XRD peaks that were characteristic of magnetite and maghemite (γ-Fe_2O_3) inverse spinel structure, according to the RRUFF database.[23] Due to the instability of magnetite, both the sets of nanoparticles are likely to contain areas of both maghemite and magnetite. Within the measured 2θ range, 6 characteristic peaks presented themselves with interplanar spacings (d-values) of 2.94, 2.52, 2.09, 1.704, 1.608, and 1.474 Å, which correspond to the crystalline planes (220), (311), (400), (422), (511), and (440), respectively. The positions of the peaks remained consistent between the samples, which indicated that both the IONP samples were similar in crystalline structure.

Analysis of the relative peak intensity and FWHM of the principle (311) peak allowed the average crystal size within the sample to be estimated using Scherrer analysis.[24] The broad, low-intensity peaks indicated the presence of nanosized crystalline domains, and the graphical measurements approximated that both the samples contained crystal sizes on the order of 10 nm. Nanoparticle size distributions, gathered from TEM imagery, validated the results gathered from the XRD. After taking measurements of the IONPs represented in the TEM images, the UC IONPs were found to have an average size of 11.5 ± 4.7 nm, while the TX IONPs had a slightly larger average size of 17.5 ± 1.0 nm (which included the TX-100 shell thickness). An image showing the TX-100 shell thickness can be found in the Supporting Information. Both of these average sizes validated the data gathered with XRD. The images also display the effects of the capping chemistry of each particle as well; the UC IONPs are shown in an agglomerated arrangement, while the TX IONPs are shown fairly uniform and monodisperse. The TX-100 works to reduce the relative surface energy and prevent agglomeration within the TX suspension, which results in increased edge separation and colloidal stability.

Vibrating sample magnetometry (VSM) and polarization analyzed SANS (PASANS) quantified the magnetic characteristics of both the IONPs, which included local particle arrangements as well as their various magnetic properties. Immediately apparent is the difference in saturation magnetization (M_s) between the two IONPs, illustrated in the hysteresis curves in the left panel of **Figure 3**. The UC and TX IONPs observed M_s values of 47.1 and 23.8 emu g^{-1}, respectively. Along with a higher M_s, the UC IONPs also had higher coercivity and remanence than the TX IONPs, which implies that their induction

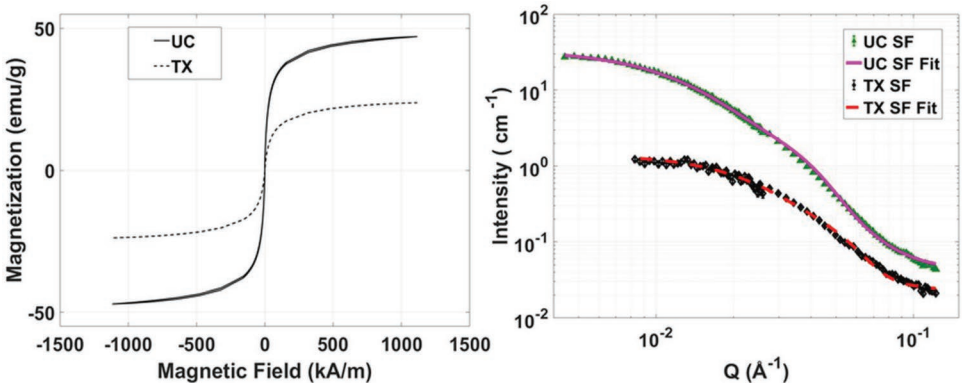

Figure 3. (left) Hysteresis curves (right) PASANS scattering intensity plots with associated fits.

heating thermal output would be much higher. The UC IONPs' lack of a capping agent and their noticeably higher M_s values indicate that they will probably cluster more easily than the TX IONPs under the influence of a high magnetic field. The PASANS spin-flip (SF) data (right panel of Figure 3) verified the higher magnetization of the UC IONPs measured with the VSM, due to having a higher intensity across the entire Q-range. The intensity of SF measurements can be roughly correlated with the magnetization of a particle system, so it is clear that the TX IONPs are noticeably less magnetic than their UC counterparts. Once fit to a pearl necklace model, the SF intensity plots for both the particle sets fit well to a magnetic correlation in the form of magnetic trimers, which consist of three interconnected spheres. This trimer model provided a basis for fitting the pearl necklace submodel used in the SANS/USANS modeling efforts; the PASANS fitting parameters can be found in the Supporting Information.

3.2. SANS and USANS Modeling and Intensity Plots

With successful incorporation into the neutron beamline(s), in situ neutron scattering data were gathered in three stages for each sample: 1) before induction heating, 2) during induction heating (alternating magnetic field strength of 30.3 kA m^{-1}), 3) after induction heating. Progressing in this manner allowed the relative change in scattering intensity to be compared within a single IONP heating cycle. Upon completion of each SANS/USANS measurement, postprocessing and background subtraction of the resulting 2D scattering patterns created a 1D intensity versus Q plot for each testing condition (**Figure 4**). Qualitative observations of each measurement in the various Q regions defined by the submodels will be discussed; more encompassing quantitative information extracted from the piecewise model will also be analyzed.

3.2.1. Observations in High-Q SANS ($Q > 4 \times 10^{-3}$ Å^{-1})

In the case of both the sets of IONPs, the range of scattering vectors larger than 0.004 Å^{-1} showed little deviation in intensity between the different heating stages in either sample; this Q-range, associated with the length scale of ≈1–150 nm is shown in the first column of Figure 4. Minimal change of intensity in the high-Q range indicates that the induction heating process is not degrading the nanoparticles' structure. A primary difference between the two particle types can be observed by the increased intensity of the UC IONPs plot at 1×10^{-2} Å^{-1}. The TEM images illustrated that the UC IONPs agglomerate much more heavily than the TX IONPs do; an increase in intensity at this points is indicative of structures in the size range of ≈60 nm, which would correlate with localized clusters of UC IONPs before heating. Measurements in the high-Q range provide little data in the case of these samples, which do not necessarily mean that the interactions within this length scale are negligible; however, the most pronounced observation can be seen in the low- to mid-Q range which corresponds with clustering on a much larger scale.

3.2.2. Observations in Mid-Q SANS (8.7×10^{-4} Å^{-1} < Q < 4×10^{-3} Å^{-1})

Initial observations of the reduced SANS data sets indicated that there was a noticeable change in scattering intensity within the mid-Q range of 8.7×10^{-4}–4×10^{-3} Å^{-1}. Transitions among the scattering profiles within this Q-range corresponded to changes in the sample structure within the physical size range of ≈150–700 nm, which coincide with the length scale occupied by large-scale IONP clusters. Examination of the increase in mid-Q scattering provides distinct evidence that our in situ method is capable of identifying long-range clustering of IONPs during induction heating.

While the high-Q scattering profiles in Figure 4 display little variance in the nanoscale regime, the data in the mid-Q region depict differences in not only the extent of the IONPs clusters but their behavior during a complete heating cycle. The UC IONPs showed an increase in intensity within the mid-Q range during induction heating; however, upon completion of the heating trial, the intensity of the "After Heat" measurement dropped below that of the "Before Heat" measurement. The TX IONPs did not have this same difference between the "Before Heat" and "After Heat" measurements; the fits were quite similar to one another. While the differences in behavior between the two IONPs can be due to a variety of factors, such as differences in capping agents and saturation magnetizations,

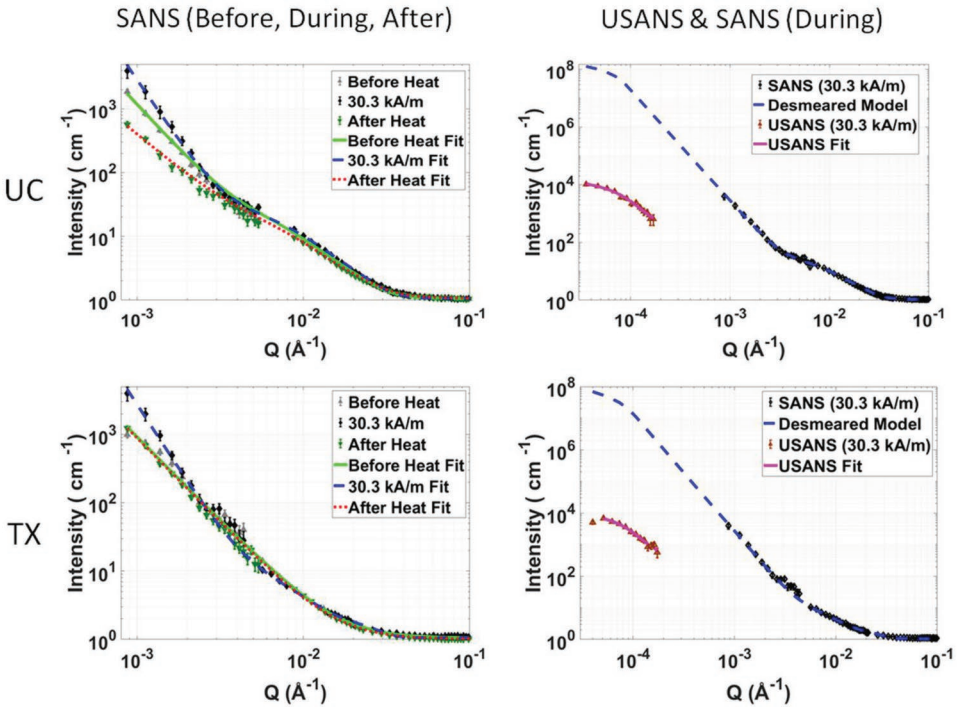

Figure 4. SANS and USANS data for the TX and UC IONPs. The first column represents the data gathered with SANS; three measurements were taken before, during, and after heating for both the particle types. The second column displays the entire model (SANS+USANS) for the "During Heating" test for both the particles. The data only extended into the USANS region when a magnetic field was applied.

the impact of said factors cannot be completely delineated from this study. It was clear, however, the use of USANS was necessary to fully resolve the size extent of the structures observed with SANS.

3.2.3. Observations in Low-Q USANS ($Q < 1.7 \times 10^{-4}$ Å^{-1})

The USANS measurements for each particle type (right column of Figure 4) progressed in a similar manner as the SANS measurements; intensity versus Q plots were generated before, during (30.3 kA m^{-1}), and after induction heating. USANS allowed for the full size of the clusters to be detected through concurrent analysis with the SANS scattering patterns. Interestingly enough, the USANS instrument only detected scattering in the ultralow Q-range during induction heating; no signal was detected either before or after heating. Because of this, only the USANS data for the "During Heating" trial were plotted for both the particle types. Due to the instrumental smearing created by the USANS instrument, called "slit smearing," the intensity is much lower than that of the SANS measurements, so the measurements were desmeared, using the reduction macros, to simulate the appearance of the data with no slit smearing. Once the USANS data were desmeared, then the entire desmeared SANS/USANS model was created, which encompasses the Q-range (0.00004–0.2 Å^{-1}). The solid line in the second column of Figure 4 illustrates the entire slit-smeared model, which combined both SANS and USANS constituents. When the data in the USANS regime were reduced and the background subtracted, a noticeable "bend" in the plot appeared around 1×10^{-4} Å^{-1}, which is characteristic of the Guinier region of the Guinier–Porod model. This occurring in the low-Q regime indicated that the nanoparticle structures detected by the SANS experiments extended into the micrometer range during induction heating, and it also indicated a finite size of these clusters at $\approx \frac{2\pi}{10^{-4}}$ Å.

3.2.4. SANS Data Fits ($Q > 8.7 \times 10^{-4}$ Å^{-1})

Detailed tables describing the fitting parameters for each test can be found in the Supporting Information. For both the IONP types, the piecewise model kept four structural parameters constant: particle radius, particle separation, number of pearls (number of nanoparticles in local group), and polydispersity (size distribution). The radii used in the fitting process corresponded to the data gathered from TEM imagery, where the TX IONPs exceeded the UC IONPs in overall size. The model introduced a Gaussian distribution of radii to account for the polydispersity in the IONPs; this value (≈0.2) for the TX IONPs correlated well with dynamic light scattering data gathered in the study by Carlton et al.[13] To account for the presence of the surfactant TX-100, the TX IONP's fit incorporated a larger edge separation for all three stages. Conversely, due to their lack of capping ligand, the UC IONPs' fit kept a much smaller edge separation. Using the data gathered in PASANS, the pearl necklace length remained constant at 3 to correlate with the existing trimer model gathered from the SF data.

Analyzing the power law component of the model (**Figure 5**) described the complexity of the IONP clusters; slopes discussed

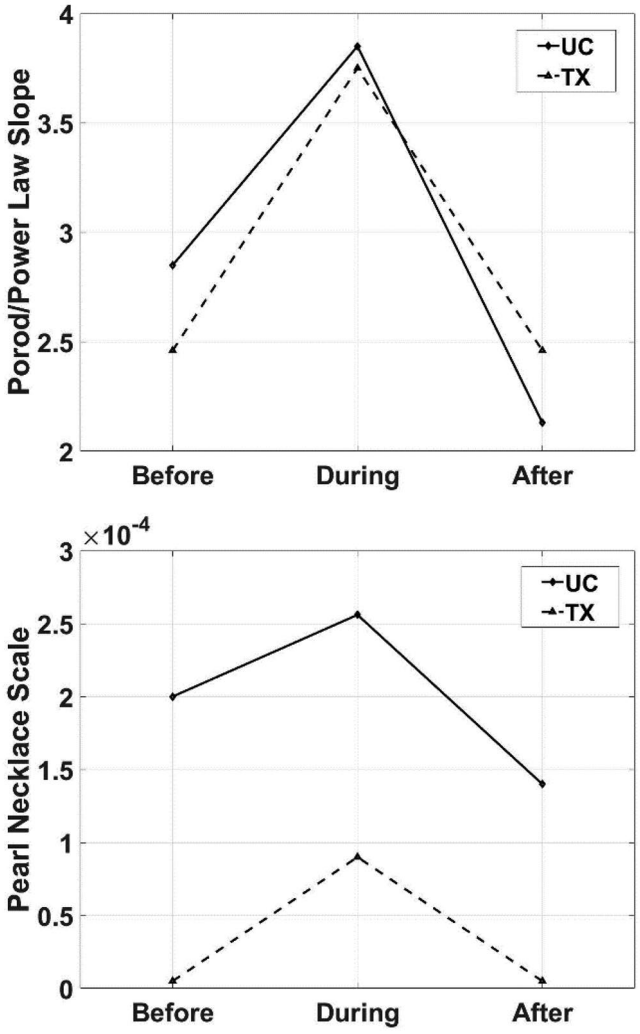

Figure 5. Shown is the progression of the power law slope (top) and pearl necklace scale (bottom) term throughout the test.

in this section correlate with extracted slopes of the mid-Q region using the Guinier–Porod model in the fitting software. The TX IONPs initially displayed a value of n between 2 and 3, at 2.45, which is a relative indication of their fractal dimension. During the induction heating process, the slope increased to 3.75, which illustrated the presence of a larger particle network and long-range chaining of IONPs in the solution. Essentially, this increase in the fractal dimension indicated that the water/particle interface transitioned to a much smoother surface during induction heating; this is consistent with the formation of larger particle clusters. After the heating process, the value returned to a similar state as before heating. Note that the "Before Heat" trial of the TX IONPs does not completely fit the piecewise model in the mid-Q range, even though the "Before Heat" and "After Heat" trials fit nearly identical. This may be attributed to the intensity beginning to plateau near 1×10^{-3} Å^{-1}, thus implying that the cluster size does not extend into the >1000 nm size regime. The UC IONPs followed a similar trend throughout the heating cycle. The slope before heating exceed that of the TX IONPs (2.85), most likely from the presence of particle aggregates due to a lack of capping agent; during heating, the slope increased to 3.85, which also surpassed the TX IONPs. Since the UC IONPs have a much higher saturation magnetization than the TX IONPs, it is reasonable to assume that they would form larger nanoparticle clusters during heating, which would result in a larger measured slope. Differing from the TX IONPs, the UC IONPs observed a drop in slope to 2.13 after heating; a decrease in the fractal dimension of this high most likely indicated a dilution of the colloidal suspension caused by IONP aggregation and settling.

Observing the relative change in the pearl necklace submodel scale allowed for the relative degree of IONP clustering to be quantified. With the polydispersity, particle size, particle separation, and the number of pearls held constant for each IONP type, the pearl necklace scale maintained proportionality to the volume fraction of the observed clusters within the IONP suspension. For both the particle sets, the scale first increased during the heating trial, and upon removal of the 30.3 kA m^{-1} alternating magnetic field (After Heat), it subsequently decreased. The rise of scale during heating corroborates the observations made with the Porod slopes: the presence of a high frequency, alternating magnetic field induces the formation of IONP clusters, which in turn increases the volume fraction of said clusters in the suspension. In the case of the TX IONPs, the scale after heating returned to a similar value as before heating, which suggests the disassembly of the particle clusters and redispersal of the IONPs back into the solution. The scale for the "After Heat" UC IONP trial cannot necessarily be compared quantitatively to the "Before Heat" trial since their Porod slopes are different; however, the decrease in both scale and power law slope after heating implies particle settling and dilution of the colloidal suspension. Basically, the UC IONPs aggregated heavily during heating, formed large clusters, and settled in the aqueous suspension, resulting in decreased colloidal stability. Greater degree of particle settling observed with the UC IONPs likely stems from their structural and magnetic properties; a higher magnetization would cause a higher magnetic attraction between neighboring IONPs, while the lack of a capping agent would encourage particle aggregation.

Utilizing SANS to experimentally determine cluster properties, such as fractal dimension, during induction heating presents a point of potential advancement in the field of IONP characterization. The majority of experiments investigating the effects of cluster geometry on the magnetic properties of colloidal systems are largely computational in nature; for one study in particular, an increase in fractal dimension of IONP aggregates resulted in a decrease in hysteresis loop size, which directly impacts particle thermal output.[25] Given that SANS can measure the particles' changing structure within an alternating magnetic field, this method provides an opportunity to expand on the aforementioned computational efforts as well as the myriad of other studies investigating IONP performance during heating. The full potential of the technique was reached when SANS was coupled with USANS, which allowed for the full size range of the IONP clusters created during induction heating to be quantified.

Table 1. Guinier–Porod model parameters. Radius of gyration is directly related to cluster size; dimension variable indicates clusters are spherical in nature.

Model parameters	UC during heating	TX during heating
Radius of gyration (r)	2.55 µm	1.988 µm
Dimension variable (s)	2.21×10^{-10}	0.365

3.2.5. USANS Data Fits ($Q < 1.7 \times 10^{-4}$ Å^{-1}) and IONP Cluster Imagery

As stated in the qualitative observations, the cluster size only extended into the USANS size regime during induction heating, so the low-Q portion of the model only fits the data gathered in the "During Heat" trial for both the IONPs. Aligning the linear power law regions of the experimental SANS and USANS data sets ensured continuity of the piecewise model for the "During Heat" trial. By constraining the slope of the linear power law region during the USANS fitting process to the same value as the power law slope from the SANS data (3.75, for TX IONPs and 3.85, for UC IONPs), the Guinier–Porod model fits quite nicely to the USANS data and provided interesting information regarding the geometry and size extent of the formed clusters. **Table 1** displays the modeled radius of gyration (r) and dimension variable (s) for each particle set during heating.

Both the particles observed fairly low dimension variables; Hammouda indicates that 3D globular objects, such as spheres, correlate with $s = 0$, while $s = 1$ corresponds to cylindrical rods.[21] The UC IONP heating trial fits to a very low dimension variable, which most likely indicates the formation of large spherical clusters during induction heating; however, the TX IONPs fit to an intermediate value between 0 and 1 (0.365). This still most likely indicates globular cluster forming, but there exist some 1D rod-like formations, such as with nanoparticle chains. The radius of gyration during induction heating also indicates that the UC IONPs exhibited larger formations than the TX IONPs. If we assume that the clusters are globular spheres, where $r = r_s\sqrt{3/5}$ (r_s is the radius of the sphere), then the diameter of the structures formed by the UC and TX IONPs are 6.6 and 5.2 µm, respectively, which is over 2 orders of magnitude larger than the particles themselves. This size range is consistent with the location of the Guinier bend discussed previously.

The micrometer size clusters delineated from the USANS fits corroborated size measurements gathered from TEM imagery. Both the particle sets were imaged with the TEM following a similar heating cycle and are represented in **Figure 6**. The TEM images of the IONPs portrayed cluster sizes on the order of >2 µm following an induction heating cycle, which is drastically different from the appearance of the particle systems before heating, shown in Figure 2. The images in Figure 6 showcase how the UC IONPs form larger more expansive aggregates than their TX IONPs counterparts, which correlates well with the small-angle scattering data in showing the presence of micrometer-size clusters for both the particle types.

While the TEM imagery was an easy comparison to aid in validating the SANS methodology, it is a poor representation of the actual cluster geometry in suspension. Since the nanoparticle samples must be dried onto the TEM grid prior to imaging, unwanted aggregation can occur, which can alter the visual appearance of the clusters. Small-angle neutron scattering methods provide a means to view a system of particles holistically and actively illustrate changing particle geometries in situ, which would prove useful for both particle fabrication and theoretical model development. Given their higher saturation magnetization and lack of a capping agent, it is not surprising that the measured size extent of the UC IONP clusters during heating would exceed that of the TX IONPs, and without methods, such as the one described herein, to directly observe nanoparticle clustering behavior during induction heating, it

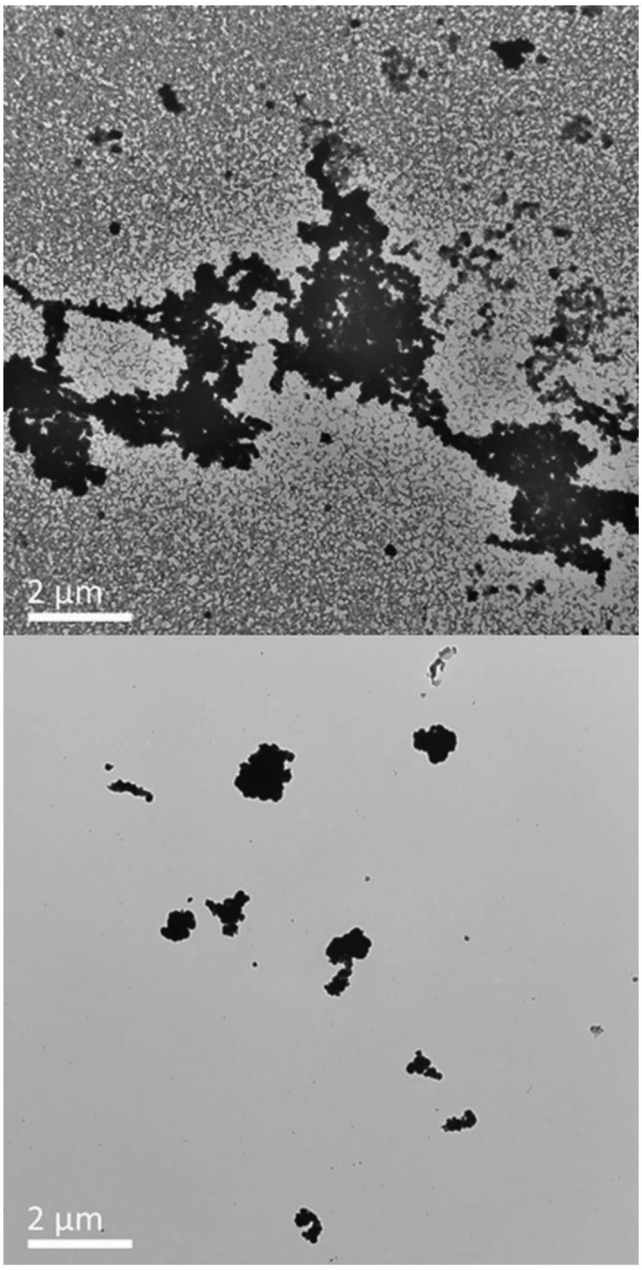

Figure 6. (top) UC IONPs after heating cycle; (bottom) TX IONPs after heating cycle.

would be difficult to get an accurate representation of how particle sets would behave in application.

4. Conclusions

Through introducing an induction coil in the NG7 SANS and BT5 USANS beamlines, a functional in situ technique of characterizing long-range IONP clustering behavior before, during, and after induction heating was developed, which makes it one of the first methods described in the literature to do so. In addition to the novel experimental environment, the SANS and USANS data were fit to a piecewise model which was able to delineate the cluster geometry over an expansive length scale from ≈2 nm to 15 µm (Q-range of 0.00004–0.302 Å^{-1}). Observations in the low- and mid-Q regions of the model indicated a relative change in IONP clustering throughout the heating cycle that varied based on particle structure. Measurements in the mid-Q region allowed for the experimental determination of the cluster fractal dimension, which indicated that both the IONPs transitioned from systems of interlinking IONP chains to clusters with relatively smooth surfaces during heating. The models for both the sets of IONPs illustrated a substantial increase in cluster size during induction heating, with the uncapped IONP suspension containing larger and more expansive clusters than their TX-100-capped counterparts. The lack of a protective shell or other stabilizing agent as well as their higher saturation magnetization attributed to the increased cluster size for the uncapped particles.

For applications, such as magnetic nanoparticle hyperthermia, particle aggregation in vivo is often not ideal to achieve satisfactory results. High frequency alternating magnetic fields present during induction heating make in situ observations of nanoparticle collective behavior difficult, so the presence of these aggregates is often not detected until afterward with microscopy. Several methods for analyzing magnetic nanoparticle performance exist, including calorimetric measurements, magnetic hysteresis analysis, and numerical simulations; however, to observe nanoparticle behavior directly is the next step in the advancement of this field of study. Implementing the technique introduced herein will add another dimension in characterizing how IONPs perform in different environments during induction heating, such as in living tissue, as well as aid in the development and synthesis of optimized magnetic nanostructures for improved hyperthermia treatments.

5. Experimental Section

IONP Synthesis: For this study, two separate nanoparticle samples were analyzed – uncapped IONPs stabilized electrostatically and IONPs capped with TX-100, a nonionic surfactant. Both the sample sets were synthesized in house and afterward were properly characterized. Upon the completion of each synthesis method, each IONP sample was diluted to a concentration of 3 mg mL^{-1} in deionized water. To ensure an even distribution of IONPs in the solution, each sample was sonicated for 15 min prior to taking a measurement.

Uncapped IONPs: The synthesis method utilized for this sample was the coprecipitation method outlined by Hariani et al. in their article which highlighted the use of magnetite (Fe_3O_4) IONPs to remove procion dye.[26] First, 16.25 and 6.35 g of $FeCl_3$ and $FeCl_2$, respectively, were dissolved in 200 mL of deoxygenated water. Upon stirring the mixture for 60 min, 2 M NaOH was added to the mixture at 30 °C, under the presence of nitrogen gas, to cause the IONPs to precipitate out, and the stirring continued for an additional 5 h at 70 °C. The IONPs were then centrifuged out and washed with deoxygenated water.

TX-100-Capped IONPs: Additional nanoparticles were synthesized using the method outlined by Mandal et al., which also used coprecipitation to create TX-100-capped magnetite nanoparticles.[27] To start, ammonium iron (III) sulfate and ammonium iron (II) sulfate were dissolved in 100 mL of 0.4 M sulfuric acid solution till the molarity of the solution with respect to the Fe(III) ion and Fe(II) ion was 0.128 and 0.064 M, respectively. The surfactant, TX-100 was added to a separate solution of 1.0 M NaOH till the concentration of the TX-100 solution was 0.01 M. The TX-100 solution was then maintained between 70 and 80 °C and stirred with a nonmagnetic stirrer while ≈25 mL of the sulfuric acid solution was dropped into it. After additional stirring for 30 min, the black IONPs settled at the bottom, were cooled to room temperature, and washed with deionized water.

Nanoparticle Characterization Techniques: XRD, TEM, and VSM characterization techniques were performed to determine the crystalline structure, size, shape, and magnetic properties of each of the nanoparticles. TEM sample preparation consisted of placing a drop of each IONP solution on a carbon-coated 200 mesh copper grid and allowing the solution to dry prior to imaging in a JEOL JEM 1011. A Rigaku Miniflex II bench-top diffractometer provided XRD measurements, which utilized Cu-Kα X-rays with a wavelength of 0.15418 nm. Each sample was analyzed between the 2θ values of 25° and 70°, and XRD patterns for the IONPs were compared to the RRUFF database for Magnetite R061111.[23] The sample preparation for XRD involved dispersing the nanoparticle solutions on a glass slide and allowing the deionized water to dry, leaving only the nanoparticles. ARkival Technology Corporation performed all VSM measurements. Similar concentrations of each IONP were suspended in deionized water and transferred to separate VSM sample holders, and hysteresis loops for each IONP sample were generated between ±1116 kA m^{-1} (±14 000 Oe).

SANS and USANS: All SANS and USANS measurements were performed at the National Institute of Standards and Technology Center for Neutron Research (NCNR) on the NG7 SANS and BT5 USANS beamlines at atmospheric pressure and room temperature.[28] All SANS measurements utilized a neutron beam with a FWHM wavelength resolution of 11.5%. For measurements within the Q-range of 0.02–0.302 Å^{-1}, neutrons of wavelength 6 Å were used, while for the range of 0.00087–0.02 Å^{-1}, neutrons of wavelength 8.09 Å were appropriated. The aperture before the sample reduced the beam diameter to 1.27 cm with a beam intensity of 7.6E5 counts s^{-1}. The USANS measurements utilized 2.4 Å neutrons with a resolution of 6% for the Q-range of 0.00004–0.0001732 Å^{-1}. All SANS and USANS data reduction was performed using the Igor Pro NCNR SANS and USANS Reduction Macros.[29] After completing the reduction process, all reduced files were modeled and fit using SasView 4.1.2.[30]

To supplement the induction heating model and the magnetic results, PASANS was used to analyze the local magnetic structure of the IONP systems; all PASANS measurements were performed on the NG7 SANS beamline. By analyzing the spin of the neutrons both before and after interacting with the sample, the magnetic contribution to the overall scattering could be unambiguously separated from the structural scattering.[31] Through observing the "SF" scattering, or the cases where the polarization of the neutrons was reversed, or "flipped," after interacting with the sample, the magnetic-only SANS data were extracted. The SF data were reduced using the same reduction macros and fitting software as with SANS.

Induction Heater Incorporation: An Ambrell EasyHeat LI 8310, 10 kW, 150–400 kHz induction heater performed all induction heating throughout the experiment; the radiofrequency (RF) coil geometry consisted of a 7-turn coil with a length of 44 mm and an inside diameter of 25 mm. Two 0.5 µF capacitors in series were used in the heater as well, which resulted in a resonant frequency of ≈303 kHz (acceptable

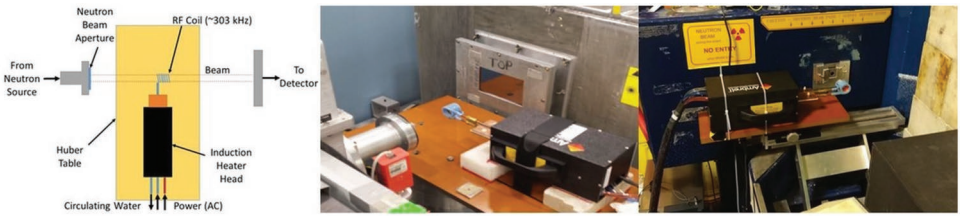

Figure 7. Diagram of the integration into the neutron beamline (left) and pictures of the experimental setups on NG-7 SANS (middle) and BT5 USANS (right).

nanoparticle heating frequency) and resulting power usage of 4.8 kW. Cooling water supplied by a Haskris R175 air-cooled 5 kW chiller controlled the internal temperature of the induction heater power supply, as well as circulated water through the RF coil.

The in situ neutron scattering observations required RF coil integration into the beamline; **Figure 7** illustrates the experimental apparatus and labels important features within the alternate sample position area on the NG-7 beamline. The induction heater coil was aligned axially with the beam direction and rested on a Huber table, to maintain constant position within the beam, and concrete blocks, to elevate the RF coil to the same level as the neutron beam. The amperage supplied to the induction heater head was input remotely with a voltage-driven control signal in the back of the power supply, which allowed subsequent heating trials to be easily programmable.

Supporting Information

Supporting Information is available from the Wiley Online Library or from the author.

Acknowledgements

Access to NG7 SANS and BT5 USANS was provided by the Center for High Resolution Neutron Scattering, a partnership between the National Institute of Standards and Technology and the National Science Foundation under Agreement No. DMR-1508249. The authors acknowledge the support of the National Institute of Standards and Technology, U.S. Department of Commerce, in providing the neutron research facilities used in this work. This work benefited from the use of the SasView application, originally developed under NSF Award No. DMR-0520547. SasView contains code developed with funding from the European Union's Horizon 2020 Research and Innovation Programme under the SINE2020 project, Grant Agreement No. 654000.

The authors would also like to thank the University of Arkansas (UA) Mechanical Engineering Department for providing travel support to NCNR, as well as the UA College of Engineering for partial project funding under the 2018 ERISF program. The authors would also like to thank Douglas Johnson, Jeff Krzywon, and Mark O'Brien for their assistance with the incorporation of the induction heater into the beamline.

All TEM imagery was provided with the assistance of the Arkansas Nano & Bio Materials Characterization Facility, and the XRD data were gathered with the help of the Nanosynthesis Laboratory at the High Density Electronics Center. The authors would like to extend thanks for their help. All magnetic hysteresis data were gathered by ARkival Technology Corporation; the authors thank them for assistance in gathering this data.

Certain commercial equipment, instruments, or materials were identified in this paper to foster understanding. Such identification did not imply recommendation or endorsement by the National Institute of Standards and Technology, nor did it imply that the materials or equipment identified were necessarily the best available for the purpose. Material deposited as Supporting Information was considered to be part of the publication and should not be submitted for republication as part of a future paper.

Conflict of Interest

The authors declare no conflict of interest.

Keywords

induction heating, iron oxide nanoparticles, long-range particle ordering, small-angle neutron scattering

Received: September 4, 2019
Revised: November 16, 2019
Published online: December 3, 2019

[1] N. Lee, D. Yoo, D. Ling, M. H. Cho, T. Hyeon, J. Cheon, *Chem. Rev.* **2015**, *115*, 10637.
[2] K. T. Nguyen, Y. L. Zhao, *Acc. Chem. Res.* **2015**, *48*, 3016.
[3] A. Hervault, N. T. K. Thanh, *Nanoscale* **2014**, *6*, 11553.
[4] a) P. Wust, B. Hildebrandt, G. Sreenivasa, B. Rau, J. Gellermann, H. Riess, R. Felix, P. M. Schlag, *Lancet Oncol.* **2002**, *3*, 487; b) J. van der Zee, G. C. van Rhoon, *Int. J. Radiat. Oncol., Biol., Phys.* **2006**, *66*, 633.
[5] C. L. Dennis, R. Ivkov, *Int. J. Hyperthermia* **2013**, *29*, 715.
[6] a) R. Muller, S. Dutz, A. Neeb, A. C. B. Cato, M. Zeisberger, *J. Magn. Magn. Mater.* **2013**, *328*, 80; b) A. S. Eggeman, S. A. Majetich, D. Farrell, Q. A. Pankhurst, *IEEE Trans. Magn.* **2007**, *43*, 2451; c) R. Hergt, S. Dutz, M. Roder, *J. Phys.: Condens. Matter* **2008**, *20*, 385214; d) S. Tong, C. A. Quinto, L. L. Zhang, P. Mohindra, G. Bao, *ACS Nano* **2017**, *11*, 6808.
[7] a) E. C. Abenojar, S. Wickramasinghe, J. Bas-Concepcion, A. C. S. Samia, *Prog. Nat. Sci.: Mater. Int.* **2016**, *26*, 440; b) Z. Nemati, J. Alonso, I. Rodrigo, R. Das, E. Garaio, J. A. Garcia, I. Orue, M. H. Phan, H. Srikanth, *J. Phys. Chem. C* **2018**, *122*, 2367.
[8] a) M. Filippousi, M. Angelakeris, M. Katsikini, E. Paloura, I. Efthimiopoulos, Y. J. Wang, D. Zambouis, G. Van Tendeloo, *J. Phys. Chem. C* **2014**, *118*, 16209; b) X. L. Liu, H. M. Fan, J. B. Yi, Y. Yang, E. S. G. Choo, J. M. Xue, D. Di Fan, J. Ding, *J. Mater. Chem.* **2012**, *22*, 8235.
[9] L. C. Branquinho, M. S. Carriao, A. S. Costa, N. Zufelato, M. H. Sousa, R. Miotto, R. Ivkov, A. F. Bakuzis, *Sci. Rep.* **2013**, *3*, 10.
[10] R. E. Rosensweig, *J. Magn. Magn. Mater.* **2002**, *252*, 370.
[11] a) C. L. Dennis, A. J. Jackson, J. A. Borchers, R. Ivkov, A. R. Foreman, J. W. Lau, E. Goernitz, C. Gruettner, *J. Appl. Phys.* **2008**, *103*, 07A319; b) C. Haase, U. Nowak, *Phys. Rev. B* **2012**, *85*, 5; c) B. Mehdaoui, R. P. Tan, A. Meffre, J. Carrey, S. Lachaize, B. Chaudret, M. Respaud, *Phys. Rev. B* **2013**, *87*, 10; d) A. Urtizberea, E. Natividad, A. Arizaga, M. Castro, A. Mediano, *J. Phys. Chem. C* **2010**, *114*, 4916; e) I. Conde-Leboran, D. Baldomir, C. Martinez-Boubeta, O. Chubykalo-Fesenko, M. D. Morales, G. Salas, D. Cabrera, J. Camarero, F. J. Teran, D. Serantes, *J. Phys. Chem. C* **2015**, *119*, 15698.

[12] R. Fu, Y. Y. Yan, C. Roberts, *AIP Adv.* **2015**, *5*, 12.
[13] H. Carlton, S. Xu, M. N. Hong, I. Begishev, D. Huitink, *J. Nanopart. Res.* **2018**, *20*, 13.
[14] S. Jeon, K. R. Hurley, J. C. Bischof, C. L. Haynes, C. J. Hogan, *Nanoscale* **2016**, *8*, 16053.
[15] T. K. Mudalige, H. Qu, D. Van Haute, S. M. Ansar, S. W. Linder, *TrAC, Trends Anal. Chem.* **2018**, *106*, 202.
[16] S. Jeon, D. R. Oberreit, G. Van Schooneyeld, Z. Gao, J. C. Bischof, C. L. Haynes, C. J. Hogan, *ACS Appl. Mater. Interfaces* **2016**, *8*, 24482.
[17] a) K. L. Krycka, A. J. Jackson, J. A. Borchers, J. Shih, R. Briber, R. Ivkov, C. Gruttner, C. L. Dennis, *J. Appl. Phys.* **2011**, *109*, 07B513; b) C. L. Dennis, K. L. Krycka, J. A. Borchers, R. D. Desautels, J. van Lierop, N. F. Huls, A. J. Jackson, C. Gruettner, R. Ivkov, *Adv. Funct. Mater.* **2015**, *25*, 4300.
[18] P. Bender, A. Gunther, D. Honecker, A. Wiedenmann, S. Disch, A. Tschope, A. Michels, R. Birringer, *Nanoscale* **2015**, *7*, 17122.
[19] a) R. Schweins, K. Huber, *Macromol. Symp.* **2004**, *211*, 25; b) S. H. Chen, J. Teixeira, *Phys. Rev. Lett.* **1986**, *57*, 2583.
[20] M. Bonini, A. Wiedenmann, P. Baglioni, *J. Appl. Crystallogr.* **2007**, *40*, s254.
[21] B. Hammouda, *J. Appl. Crystallogr.* **2010**, *43*, 716.
[22] B. Hammouda, *Probing Nanoscale Structures - The SANS Toolbox,* National Institute of Standards and Technology, Gaithersburg, MD **2016**.
[23] B. Lafuente, R. T. Downs, H. Yang, N. Stone, in *Highlights in Mineralogical Crystallography* (Ed: W. De Gruyter), Berlin, Germany **2015**, p. 1.
[24] M. A. R. Miranda, J. M. Sasaki, *Acta Crystallogr., Sect. A: Found. Adv.* **2018**, *74*, 54.
[25] a) O. Hovorka, *J. Phys. D: Appl. Phys.* **2017**, *50*, 044004; b) R. Fu, Y. Y. Yan, C. Roberts, Z. Y. Liu, Y. Y. Chen, *Sci. Rep.* **2018**, *8*, 10.
[26] P. L. Hariani, M. Faizal, D. Setiabudidaya, *Int. J. Environ. Sci. Dev.* **2013**, *4*, 336.
[27] M. Mandal, S. Kundu, S. K. Ghosh, S. Panigrahi, T. K. Sau, S. M. Yusuf, T. Pal, *J. Colloid Interface Sci.* **2005**, *286*, 187.
[28] C. J. Glinka, J. G. Barker, B. Hammouda, S. Krueger, J. J. Moyer, W. J. Orts, *J. Appl. Crystallogr.* **1998**, *31*, 430.
[29] S. R. Kline, *J. Appl. Crystallogr.* **2006**, *39*, 895.
[30] P. Butler, M. Doucet, A. Jackson, S. King, SasView for Small-Angle Scattering Analysis, https://www.sasview.org/ (accessed: June 2018).
[31] K. L. Krycka, J. J. Rhyne, S. D. Oberdick, A. M. Abdelgawad, J. A. Borchers, Y. Ijiri, S. A. Majetich, J. W. Lynn, *New J. Phys.* **2018**, *20*, 123020.

